Journal of Magnetic Resonance **146,** 1–13 (2000)
doi:10.1006/jmre.2000.2096, available online at http://www.idealibrary.com on IDEAL®

Numerical Studies of Intermolecular Multiple Quantum Coherences: High-Resolution NMR in Inhomogeneous Fields and Contrast Enhancement in MRI

Sean Garrett-Roe and Warren S. Warren

Department of Chemistry, Princeton University, Princeton, New Jersey 08544-1009

Received August 18, 1999; revised March 29, 2000

A fast, efficient numerical algorithm is used to study intermolecular zero-quantum coherences (iZQCs) and double-quantum coherences (iDQCs) in two applications where the three-dimensional structure of the magnetization is important: high-resolution NMR in inhomogeneous fields and contrast enhancement in MRI. Simulations with up to 2 million coupled volume elements (256 × 256 × 32) show that iZQCs can significantly narrow linewidths in the indirectly detected dimension of systems with inhomogeneous fields and explore the effects of shape and orientation of the inhomogeneities. In addition, this study shows that MR images from iZQC and iDQC CRAZED pulse sequences contain fundamentally new contrast, and a modified CRAZED pulse sequence (modCRAZED) can isolate the contrast from chemically inequivalent spins.

I. INTRODUCTION

Dipolar couplings between distant spins produce additional peaks in the indirectly detected dimension in solution two-dimensional NMR experiments (*1–3*). Such peaks can be understood in two superficially quite different frameworks. The dipolar field can be reduced (by a mean-field treatment) to a magnetic field correction at each spin, traditionally called the dipolar demagnetizing field (*4*), but perhaps more accurately called the distant-dipole field (*5*) (we will use the abbreviation "DDF" here). This approach, commonly called the "classical" or "mean-field" treatment (*1, 6*), produces a nonlinear version of the Bloch equations and has been used in a wide variety of different applications (*1, 4, 7*). Alternatively, the dipolar couplings can be explicitly retained. In this case (which we have generally called the "quantum" or "coupled-spin" treatment) the signal arises entirely from intermolecular multiple-quantum coherences (iMQCs) (*6, 8*) involving spins with a macroscopic separation.

In solution, these two treatments generally give identical results (*6, 9*); Reference (*10*) shows that the largest expected error is about 10^{-6} of the total magnetization. Unfortunately, analytical results are generally restricted to uniformly magnetized but nonspherical samples (*6, 9*) or to magnetization modulated in one dimension over a much shorter distance than any variations in resonance frequency or magnetization density, and in many interesting applications these assumptions will be violated. For example, a tumor might have a different resonance frequency than surrounding tissue because of the differences in oxygen concentration; it might also have different magnetization density or relaxation times. As another example, an electromagnet (such as the 25-T Keck magnet at NHFML, with a 1066-MHz proton resonance frequency) will typically have $>$1 kHz residual inhomogeneity, and the field will drift as well. The DDF now becomes a complex and time-dependent function of the magnetization distribution, which robs the classical treatment of any real intuitive value. The quantum treatment retains some (qualitative) predictive power in this limit: intermolecular zero-quantum coherences (iZQCs) are expected to refocus the long-range component of the inhomogeneous broadening or to monitor local resonance frequency gradients. Experiments have shown that iZQCs can give homogeneous NMR spectra even in inhomogeneous magnetic fields (*11*) and can provide MRI contrast enhancement both *in vivo* and *in vitro* (*12*). However, quantitative predictions of signal intensity in this limit would be difficult and have not been published.

Recently Enss *et al.* have proposed an efficient numerical method that predicts dipolar field effects in structured media (*13*). Here we use this method to present the first quantitative analysis of the expected line narrowing from iZQCs in inhomogeneous fields and explore the effects of shape and orientation of the inhomogeneities. In addition, this study shows that MR images from appropriately designed iZQC and iDQC CRAZED pulse sequences contain fundamentally new contrast, and a modified CRAZED pulse sequence (modCRAZED) can isolate the contrast from chemically inequivalent spins.

II. PROPERTIES OF INTERMOLECULAR MULTIPLE-QUANTUM COHERENCES

The properties of *intra*molecular multiple-quantum coherences have been known for some time, but their application has

1090-7807/00 $35.00

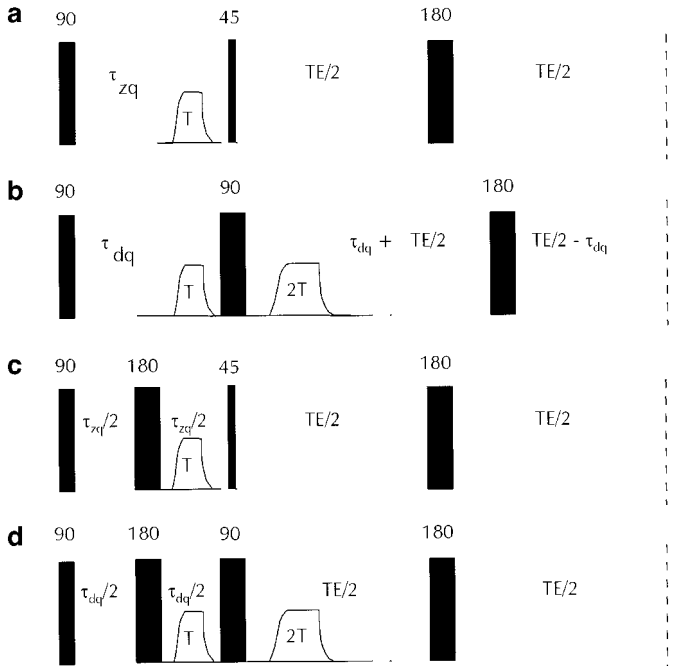

FIG. 1. a: Diagram of the iZQC CRAZED (or HOMOGENIZED) pulse sequence, used in both imaging and spectroscopy simulations in this paper. Gradient pulses are shown in white and RF pulses in black. b: Diagram of the iDQC CRAZED sequence. Note that the final 180 pulse does not bisect the final time interval; the iDQC evolution time τ_{dq} must be balanced by a single-quantum evolution time of $2*\tau_{dq}$ as discussed in the text. c and d: Modified versions of the iZQC and iDQC sequences (respectively), which refocus chemical shift evolution in τ_{zq} or τ_{dq}. These "modCRAZED" sequences eliminate chemical shift evolution as a contrast mechanism.

been limited in solution to systems that are *J*-coupled with spins separated by distances on the order of Angstroms. *Inter*-molecular multiple-quantum coherences, however, which use the long-range dipolar coupling between distant spins, can be observed in nearly all NMR samples and can probe even macroscopic properties. Applying iZQCs to high-resolution NMR in inhomogeneous fields allows measurement of the relative inhomogeneity between two spins, rather than the total inhomogeneity of the system, which could give a significant line narrowing. In MR imaging, the evolution of iZQCs at the difference in chemical shift between two spins introduces a fundamentally new and potentially useful source of contrast.

Figure 1 gives the iZQC and iDQC CRAZED and modified CRAZED pulse sequences. In this section we briefly review the application of the quantum picture for such sequences, because as noted earlier the classical picture does not give any simple results for highly modulated magnetization. The quantum picture for how the CRAZED pulse sequence can create signal from multiple-quantum operators after only two pulses begins by dropping the usual high-temperature approximation to the density matrix. Reference (*6*) starts from the exact density matrix,

$$\rho_{\mathrm{eq}} = 2^{-(N+M)} \prod_{i}^{N} (1 - \Im_I I_{zi}) \times \prod_{k}^{M} (1 - \Im_S S_k), \qquad [1]$$

where $\Im_I = 2 \tanh(\hbar\omega_I/2kT)$ and $\Im_S = 2 \tanh(\hbar\omega_S/2kT)$. Although Eq. [1] is entirely general, for this paper the *I* and *S* spins have the same gyromagnetic ratio but different Larmor frequencies (i.e., $\omega_I \neq \omega_S$). In this description, the equilibrium density matrix contains multiple spin terms such as $I_{zi}I_{zj}$ (as well as higher order terms), where the *i* and *j* indices indicate spins on separate molecules.

Reference (*6*) analytically solves the double-quantum coherence case of the CRAZED pulse sequence including all multispin terms, but Ref. (*2*) shows that even a two-spin calculation gives a fairly accurate prediction on a short time scale and gives the essential insight into the spins' behavior (which is all we desire here). The first RF pulse rotates the two-spin magnetization into the transverse plane, creating iDQCs and iZQCs, for example

$$I_{zi}S_{zj} \xrightarrow{90_x} I_{yi}S_{yj}. \qquad [2]$$

Because the gradient in t_1 is unmatched in t_2, only the iZQC terms in t_1 will survive spatial averaging. The zero-quantum operators have two symmetries,

$$\begin{aligned} I_i^+S_k^- + I_i^-S_k^+ &= 2[I_{xi}S_{xk} + I_{yi}S_{yk}] \\ I_i^+S_k^- - I_i^-S_k^+ &= 2i[I_{yi}S_{xk} - I_{xi}S_{yk}]. \end{aligned} \qquad [3]$$

Chemical shift evolution in t_1 gives

$$\begin{aligned} &[I_i^+S_k^- + I_i^-S_k^+]\cos(t_1(\Delta\omega_I - \Delta\omega_S)) \\ &\quad = 2[I_{xi}S_{xk} + I_{yi}S_{yk}]\cos(t_1(\Delta\omega_I - \Delta\omega_S)) \\ &[I_i^+S_k^- - I_i^-S_k^+]\sin(t_1(\Delta\omega_I - \Delta\omega_S)) \\ &\quad = 2i[I_{yi}S_{xk} - I_{xi}S_{yk}]\sin(t_1(\Delta\omega_I - \Delta\omega_S)). \end{aligned} \qquad [4]$$

The dipolar Hamiltonian can only make single-quantum, multispin terms observable, so the terms that will lead to observable magnetization after the second RF pulse (45_x) are

$$\begin{cases} I_{xi}I_{xj} + I_{yi}I_{yj} \\ I_{xi}I_{yj} - I_{yi}I_{xj} \\ I_{xi}S_{xk} + I_{yi}S_{yk} \\ I_{xi}S_{yk} - I_{yi}S_{xk} \end{cases} \xrightarrow{45_x} \begin{cases} I_{yi}I_{zj} + I_{zi}I_{yj} \\ I_{xi}I_{zj} - I_{xi}I_{zj} \\ I_{yi}S_{zk} + I_{zi}S_{yk} \\ I_{xi}S_{zk} - I_{zi}S_{xk}. \end{cases} \qquad [5]$$

Commutation with the dipolar Hamiltonian (H_{dij}) gives

$$\begin{cases} I_{yi}I_{zj} + I_{zi}I_{yj} \\ I_{xi}I_{zj} - I_{zi}I_{xj} \\ I_{yi}S_{zk} + I_{zi}S_{yk} \\ I_{xi}S_{zk} - I_{zi}S_{xk} \end{cases} \xrightarrow{H_{dij}} \begin{cases} I_{xi} + I_{xj} \\ I_{yi} - I_{yj} \\ I_{xi} + S_{xj} \\ I_{yi} - S_{yj}. \end{cases} \quad [6]$$

Including the chemical shift evolution in t_1, the final result is

$$\left.\begin{matrix} (I_{xi} + I_{xj})\cos(0) = (I_{xi} + I_{xj}) \\ (I_{yi} - I_{yj})\sin(0) = 0 \end{matrix}\right\} \text{axial peak}$$

$$\left.\begin{matrix} (I_{xi} + S_{xj})\cos(t_1(\Delta\omega_I - \Delta\omega_S)) \\ (I_{yi} - S_{yj})\sin(t_1(\Delta\omega_I - \Delta\omega_S)) \end{matrix}\right\} \text{cross peak.} \quad [7]$$

This signal is then modulated by chemical shift evolution in t_2. There is also a symmetric contribution from the S spins (found by reversing I and S). The signal from spins with the same Larmor frequency (the top lines of Eq. [7]) has an evolution frequency of 0 Hz and is called an axial peak. The signal from spins with different frequencies has a nonzero evolution frequency and is called a cross peak.

The only difference the modCRAZED pulse sequence introduces is a π refocusing pulse in the center of t_1. This pulse refocuses all chemical shift evolution in t_1, giving

$$\left.\begin{matrix} (I_{xi} + I_{xj})\cos(0) = (I_{xi} + I_{xj}) \\ (I_{yi} - I_{yj})\sin(0) = 0 \end{matrix}\right\} \text{axial peak}$$

$$\left.\begin{matrix} (I_{xi} + S_{xj})\cos(0) = (I_{xi} + S_{xj}) \\ (I_{yi} - S_{yj})\sin(0) = (I_{yi} - S_{yj}) \end{matrix}\right\} \text{cross peak.} \quad [8]$$

Thus subtracting the iZQC CRAZED signal from the modCRAZED signal allows only the cross peak to survive. The axial peaks cancel exactly, leaving only

$$\left.\begin{matrix} (I_{xi} + S_{xj})(1 - \cos(t_1(\Delta\omega_I - \Delta\omega_S))) \\ (I_{yi} - S_{yj})(-\sin(t_1(\Delta\omega_I - \Delta\omega_S))) \end{matrix}\right\} \text{cross peak.} \quad [9]$$

This simple two-spin calculation suggests that the real part of the signal will have a maximum when the difference in chemical shift evolution in t_1 is π rad. If, for example, the difference in chemical shift is 25 Hz, the maximum signal will occur at $t_1 = 20$ ms.

A. Phase Cycling

Phase cycling compensates for artifacts with physical origins as well as artifacts inherent in the simulation and provides a good example of the use of the quantum picture. In general, there are three schemes for phase cycling the CRAZED sequence. The first two handle residual magnetization while the third handles relaxation artifacts in τ_{zq}. In experiments, residual magnetization is largely a product of an imperfect excitation pulse (i.e., the first pulse is not exactly $\pi/2$ across the entire sample). In simulations, though, pulse accuracy is not a problem, and residual magnetization springs from the limited sample size and few helices of magnetization across the sample. When the sample is small, any chemical shift distribution (one of the properties we are interested in investigating) will partially unwind the magnetization helix, giving some residual single-quantum signal.

This residual magnetization can be eliminated by phase cycling the first RF pulse or the correlation gradient. Changing the sign of the first RF pulse from $+90$ to -90 leaves the iMQC signal unchanged but reverses the sign of the residual magnetization:

$$\left.\begin{matrix} I_z \xrightarrow{+90_x} +I_y \\ I_z \xrightarrow{-90_x} -I_y \end{matrix}\right\} = 0, \quad [10]$$

but

$$I_{zi}I_{zj} \xrightarrow{\theta_x} (I_{zi}\cos(\theta) + I_{yi}\sin(\theta)) \times (I_{zj}\cos(\theta) + I_{yj}\sin(\theta)), \quad [11]$$

which shows that

$$\left.\begin{matrix} I_{zi}I_{zj} \xrightarrow{\theta = +90_x} (+I_{yi})(+I_{yj}) = I_{yi}I_{yj} \\ I_{zi}I_{zj} \xrightarrow{\theta = -90_x} (-I_{yi})(-I_{yj}) = I_{yi}I_{yj} \end{matrix}\right\} = 2I_{yi}I_{yj}. \quad [12]$$

Coadding these signals eliminates the artifacts.

Alternately, Ref. (*2*) showed that changing the gradient direction from z to x or y leaves the residual magnetization unchanged but multiplies the DDF by $-\frac{1}{2}$ (see also Eq. [24] below). For short evolution times, i.e., when $\gamma|\mathbf{B}_d|t_2 \leq 1$ (a limit often achieved in practice), the signal is proportional to $\mathbf{B}_d$. Because changing the gradient direction does not change the residual magnetization, subtracting these signals removes residual magnetization effects but retains the zero-quantum signal.

Relaxation during τ_{zq} also creates significant artifacts. T_1 effects can be removed by a third phase cycling scheme, i.e., by changing the second RF pulse from $\theta = 45_x$ to -135_x, which again reverses the single-quantum signal, but does not affect the axial peak of the iZQC. Examining the real and imaginary

parts of the result shows some of the details of this process. If T_1 has created some z-magnetization at the end of τ_{zq}, then

$$I_z \xrightarrow{\theta_x} I_z\cos\,\theta + I_y\sin\,\theta. \qquad [13]$$

Adding the results from $\theta = 45_x$ and -135_x shows that

$$I_z(\cos(45) + \cos(-135)) + I_y(\sin(45) + \sin(-135)) = 0. \qquad [14]$$

The effect on two-spin terms is quite different, however. Again, zero-quantum operators have two expansions.

$$I^+S^- + I^-S^+ = 2[I_xS_x + I_yS_y]$$
$$I^+S^- - I^-S^+ = 2i[I_yS_x - I_xS_y] \qquad [15]$$

Phase cycling the second RF pulse effects these two expressions differently. For the real pair, an arbitrary θ_x pulse creates

$$I_xS_x + I_yS_y \xrightarrow{\theta_x} I_xS_x + (I_y\cos\,\theta - I_z\sin\,\theta)(S_y\cos\,\theta - S_z\sin\,\theta)$$
$$= I_vS_z\sin\,\theta\,\cos\,\theta + I_zS_y\sin\,\theta\,\cos\,\theta + \text{unobservable terms.} \qquad [16]$$

Only two-spin, single-quantum terms can be made observable by one commutation with the dipolar Hamiltonian, so three of the five terms lead to no observable magnetization. Because the product sin θ cos θ is positive when $\theta_x = 45$ and -135, this phase cycling preserves the iZQC from these terms. The imaginary pair, on the other hand, under a θ_x pulse becomes

$$I_yS_x - I_xS_y \xrightarrow{\theta_x} (I_y\cos\,\theta - I_z\sin\,\theta)S_x - I_x(S_y\cos\,\theta - S_z\sin\,\theta)$$
$$= I_xS_z\sin\,\theta - I_zS_x\sin\,\theta + \text{unobservable terms.} \qquad [17]$$

Adding $\theta_x = 45$ and -135 shows that these iZQC contributions from the I and S spins evolve in opposite senses during t_1.

It is worth noting the symmetry properties of these two expansions of the zero-quantum operators. The real pair, in this pulse sequence, leads to the real component of the observed signal. For example,

$$I_yS_z \xrightarrow{H_{dij}} I_x. \qquad [18]$$

The imaginary pair leads to the imaginary component of the signal

$$I_xS_z \xrightarrow{H_{dij}} I_y. \qquad [19]$$

The second line in Eq. [15] has the same symmetry properties as I_z because

$$I_z = -i[I_x, I_y]. \qquad [20]$$

For this reason, the same phase cycling scheme that removes I_z could remove the imaginary component of the CRAZED signal, Eq. [17], except that the signals on I and S spins have different modulations in t_2 in the latter case. If the evolution in t_2 is refocused, however, these imaginary signals will cancel.

Although RF and gradient methods both are effective, these simulations use only the RF methods.

III. SIMULATION PROGRAM

The quantum formalism gives a sense of how the pulse sequences will behave, but the classical, Bloch equation formalism is much more efficient for numerical calculations. The equation of motion for the magnetization vector, $\mathbf{M}(\mathbf{r}, t)$, is

$$\frac{\partial\mathbf{M}(\mathbf{r}, t)}{\partial t} = \gamma\mathbf{M}(\mathbf{r}) \times \left\{\left[\frac{\Delta\omega}{\gamma}\,\hat{\mathbf{z}} + G(\hat{\mathbf{s}}\cdot\mathbf{r})\hat{\mathbf{s}}\right] + \mathbf{B}_r(\mathbf{r}) + \mathbf{B}_d(\mathbf{r})\right\} - \frac{M_x(\mathbf{r})\hat{\mathbf{x}} + M_y(\mathbf{r})\hat{\mathbf{y}}}{T_2(\mathbf{r})} + \frac{M_0(r) - M_z(\mathbf{r})\hat{\mathbf{z}}}{T_1(\mathbf{r})} - D\nabla^2\mathbf{M}(\mathbf{r}, t). \qquad [21]$$

This is a partial differential equation (PDE) that must be integrated from $t = 0$ to t_{final}. Most of the components of this equation are relatively easy to handle, but the DDF and diffusion require some thought to calculate efficiently.

Equation [21] presents a set of nonlinear, coupled equations. Because these equations are nonlinear, the result of each time step depends explicitly on the starting conditions. Dealing with the terms that create this coupling in a smart way will vastly improve calculation time. For chemical shift, applied gradients, and relaxation alone, each PDE, expressed as a function of $\mathbf{r}$,

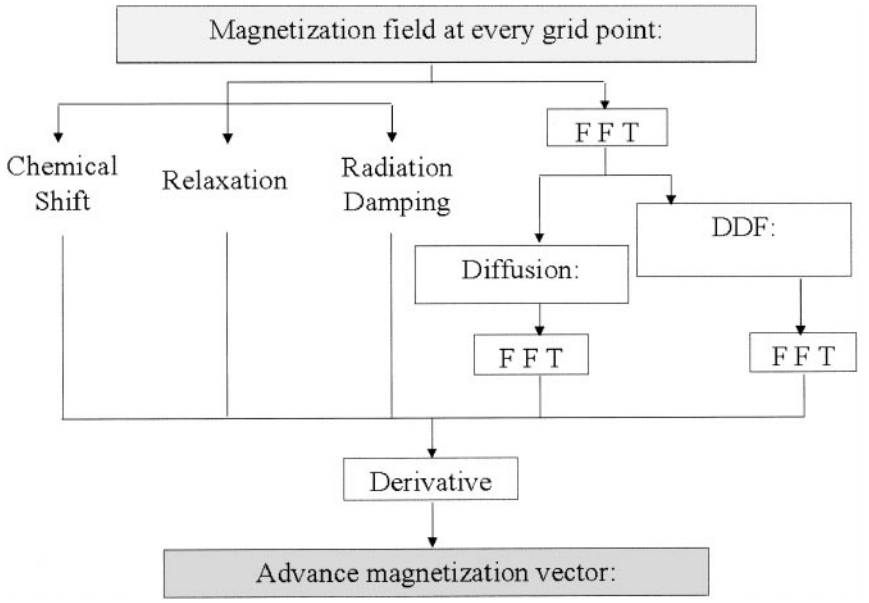

FIG. 2. Schematic of the algorithm that allows efficient numerical calculation of DDF effects in inhomogeneous systems by switching between real and Fourier spaces.

is unrelated to the others, so these can be calculated directly. The radiation damping field is given by

$$\mathbf{B}_{\mathrm{r}}(\mathbf{r}) = \frac{\langle M_y \rangle}{\gamma M_0 \tau_{\mathrm{r}}} \hat{\mathbf{x}} + \frac{\langle M_x \rangle}{\gamma M_0 \tau_{\mathrm{r}}} \hat{\mathbf{y}}, \qquad [22]$$

where $\tau_{\mathrm{r}} = 1/(2\pi\eta M_0 Q\gamma)$, η is the filling factor, and Q is the probe Q-factor. To compute radiation damping, finding the average magnetization in the transverse plane $\langle M_x \rangle$ and $\langle M_y \rangle$ is the only necessary calculation. While this term is nonlocal, it is inexpensive (in terms of computer memory and CPU time) to calculate it because $\mathbf{B}_{\mathrm{r}}(\mathbf{r})$ needs to be calculated only once per time step. If the coil can be assumed to give a homogeneous RF field, the radiation damping field is uniform across the sample.

The expressions for the DDF and diffusion, however, rely explicitly on each point's surroundings. The complete expression for the dipolar demagnetizing field is

$$\mathbf{B}_{\mathrm{d}}(\mathbf{r}) = \frac{\mu_0}{4\pi} \int d\mathbf{r}' \, \frac{1 - 3\cos^2\theta_{\mathrm{rr}'}}{2|\mathbf{r} - \mathbf{r}'|^3} [3M_z(\mathbf{r}')\hat{\mathbf{z}} - \mathbf{M}(\mathbf{r}')], \qquad [23]$$

which is quite expensive to calculate in real-space because it is nonlocal. Finding $\mathbf{B}_{\mathrm{d}}(\mathbf{r})$ at each point requires integrating over the magnetization of every other point and then repeating *for all other points.* Similarly, the effect of diffusion at each point depends on neighboring points. Finding a solution to this set of coupled equations is very expensive in processor time and computer memory.

Deville *et al.* [4] noted that this expression for the DDF simplifies in k-space. In essence, the DDF depends on the modulation of the magnetization in a simple way, where it is a complicated expression in position.

$$\mathbf{B}_{\mathrm{d}}(\mathbf{k}) = \frac{\mu_0}{6} [3(\hat{\mathbf{k}} \cdot \hat{\mathbf{z}})^2 - 1][3M_z(\mathbf{k})\hat{\mathbf{z}} - \mathbf{M}(\mathbf{k})] \qquad [24]$$

The k-space representation gives a set of local, uncoupled coordinates in which to calculate the DDF. Representing the magnetization in this set of coordinates by discrete fast Fourier transformation simplifies the calculation of the DDF immensely. In addition, diffusion has a simple closed form in k-space,

$$D\nabla^2\mathbf{M}(\mathbf{r}) \xrightarrow{\text{Fourier transform}} -Dk^2\mathbf{M}(\mathbf{k}). \qquad [25]$$

Unfortunately, in k-space, chemical shift and relaxation are no longer local expressions, so performing the entire calculation in k-space is no more efficient than a calculation in real-space. The solution to this quandary is to Fourier transform the magnetization from real-space to k-space, calculate the dipolar field and diffusion in their local coordinates, and then take the result and transform back to real-space. The final result is a vast speedup—two three-dimensional Fourier transformations in the place of the coupled equations of motion under the DDF. Figure 2 gives a schematic of the numerical algorithm.

This approach to the calculation brings with it several limitations and artifacts, none of which is overwhelming, but care

should be taken. The first of these is a singularity at $\mathbf{k} = 0$ in the calculation of the DDF (Eq. [24]). The DDF depends on the dot product $\hat{\mathbf{k}} \cdot \hat{\mathbf{z}}$ which is undefined when $\mathbf{k} = 0$. The $\mathbf{B}_d$ ($\mathbf{k} = 0$) component corresponds to the contribution of the average magnetization of the sample to the dipolar field. If the sample is a sphere, this contribution is strictly zero, and there is no error ignoring the point $\mathbf{k} = 0$ in our calculation. When the sample is not spherical, ignoring the contribution of the average magnetization is an approximation, but, as long as the sample remains nearly cubic, it is a reasonable one. Reference (*13*) corrects Eq. [24] for these residual effects, but the correction is small in most CRAZED-type experiments.

The next requirement on the calculation springs from the periodic nature of the DFFT. Taking the discrete Fourier transform of a sample is mathematically equivalent to replacing the sample with a periodically repeated array of samples. To prevent anomalous edge effects, the sample must be surrounded by empty space. So as long as this zero-padding creates a "period" that is sufficiently long, the artifacts will be minimal. We have recently shown that the error due to edge effects and limited sample size are quite minimal (*13*).

A fifth-order Cash–Karp Runge–Kutta formula performs the integrations in the majority of these calculations. This method varies the step size based on an estimate of truncation error, balancing calculation speed and numerical accuracy. The calculations are generally performed in double precision, and the truncation error is kept below 10^{-5}. Memory requirements limit sample size to approximately 64 by 64 by 32 grid points (between 1 and 10 h, on average, using 77 Mbytes of memory) for one-component systems or 32 by 32 by 64 grid points for systems with two spin species (different gyromagnetic ratios, for example). When calculations are single precision and use the less accurate, slower Euler method integration, however, sample sizes of up to 256 by 256 by 32 become possible in a reasonable amount of time (approximately 20 h using 120 Mbytes of memory).

The code for these simulations was written in Fortran and C, with several user-interface applications in the scripting language Python. Silicon Graphics Indigo-2 XZ workstations ran these calculations. These took between 1 and 38 h to complete, depending on sample size, number of time steps, and, most importantly, the chemical shift distribution. When there is a large distribution of chemical shifts in the sample, the integration step size decreases in order to maintain numerical accuracy, and the calculation time increases concomitantly. Matlab provided postcalculation processing and visualization tools.

In all cases, global parameters (uniform for all points in the sample) included temperature, magnetic field, radiation damping time, and gyromagnetic ratio (up to two kinds of spins available). Five parameters could be set arbitrarily for each point in sample including spin density, diffusion constant, T_1, T_2, and chemical shift.

IV. NMR IN INHOMOGENEOUS FIELDS

The first set of simulations examines iZQC as applied to high-resolution NMR in inhomogeneous magnetic fields. For example, in an electromagnet iZQCs can significantly narrow linewidths in the indirectly detected dimension of samples with inhomogeneous broadening, as seen in preliminary experiments (*11*). We wish to quantify the expected narrowing for different spatial distributions.

For these simulations, the sample is a 24-point cube surrounded by 4 points of empty space. Each side of the sample is approximately 1 mm long. The zero-quantum coherence time, τ_{zq}, was incremented in 3.33-ms steps for a total 192-ms acquisition time. The residual inhomogeneous broadening implies that full two-dimensional spectra can be replaced with one-dimensional spectra in the indirectly detected dimension, since only points near the peak of the echo have significant signal. Two π pulses refocus the signal in t_2, and only t_1 is varied during the experiment. In a general two-dimensional experiment, the signal observed in t_2 takes the form

$$S = \sum_i S_i(t_1, t_2) = \sum_i f_i(t_1, t_2) \cdot \exp(i\Delta\omega_i t_2), \qquad [26]$$

where S_i is the signal from the ith spin species, $f_i(t_1, t_2)$ is an arbitrary function of t_1 and t_2, and $\Delta\omega_i$ is the chemical shift (in the rotating frame). In this specific case, the π pulses in t_2 refocus the effects of chemical shift evolution, giving

$$S = \sum_i f_i(t_1, t_2) \cdot \exp(0) = C(t_2) \cdot f_i(t_1). \qquad [27]$$

Here $C(t_2)$ is a constant determined by the refocusing point chosen in t_2. In this way, the two-dimensional time domain is a delta function in t_2 and a periodic function in t_1. In the case of iZQCs, the amplitude constant $C(t_2)$ represents the competition between the growing signal from the action of multiple commutations with the dipolar Hamiltonian and damping effects of relaxation. The first of these increases in amplitude up to a maximum at 2.6 τ_d, where τ_d is the dipolar demagnetizing time (*11*), but is simultaneously reduced by both T_1 and T_2. In these samples T_1 and T_2 were set at the common experimental values of 1 s each. The final point chosen in t_2 was the observed maximum in the signal.

Three different types of samples and several inhomogeneity distributions were investigated. Each sample type presents a more ambitious experiment with increasing demands on iZQC CRAZED pulse sequence performance. The first sample is a one-component system, the second is an equimolar, two-component system, and third is a solvent–solute two-component system (111 M solvent, 1 M solute). The second two systems consist of homonuclear spins with a 25-Hz chemical shift difference.

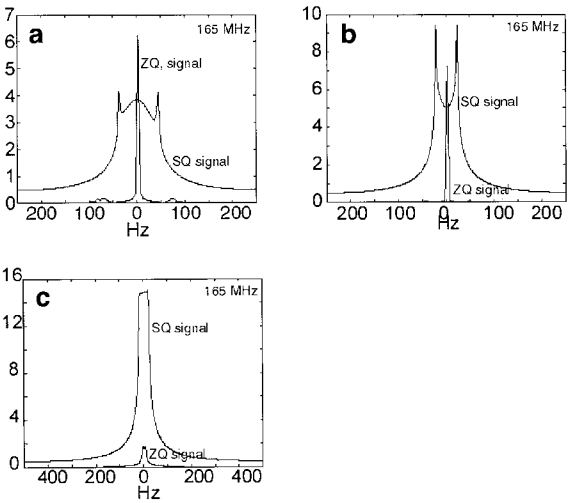

FIG. 3. Comparisons of SQ and iZQC CRAZED linewidths for a one-component system. These samples have inhomogeneous broadening (a) linear along the z-axis, (b) Gaussian along the z-axis, and (c) linear along the x-axis. In (a) and (b) the iZQC CRAZED produces linewidths of 6 Hz (FWHM) while the conventional spectrum linewidth is ~50 Hz. In (c) the iZQC CRAZED linewidth is >20 Hz. See text for details.

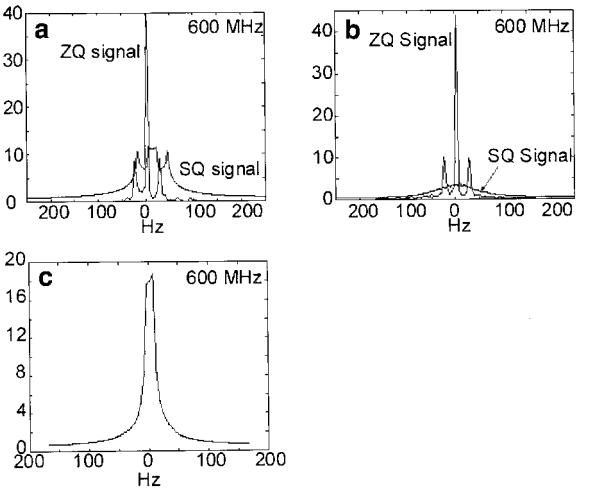

FIG. 4. Comparisons of conventional spectra with iZQC CRAZED for an equimolar two-component system, component one 0 Hz, component two 25 Hz. These samples have inhomogeneous broadening (a) linear along the z-axis (50 Hz), (b) Gaussian along the z-axis (25 Hz standard deviation), and (c) linear along the x-axis (50 Hz). In (a) and (b) the iZQC CRAZED cross-peaks are clearly resolved. In (c) no cross peak is resolvable due to the x component of the spatial modulation.

The inhomogeneities are modeled as either a linear or a Gaussian chemical shift inhomogeneity along either the z- or the x-axis. The linear inhomogeneous broadening is, essentially, a permanent gradient along the axis of choice, and all points in a slice normal to that axis have the same resonance frequency. The Gaussian distribution is made by generating a string of numbers with a normal distribution around zero and standard deviation, $\sigma = 25$ Hz, via a random number generator. This one-dimensional array is mapped onto the volume of the sample by first increasing the x index, then y, and, last, z. Because of this construction, there is a chemical offset gradient of approximately 0.1 Hz across the x-direction, 2 Hz across the y-direction, and roughly 50 Hz across the z-direction. Because the z-modulation is much stronger (an order of magnitude greater) than the other offsets, this adequately approximates a Gaussian distribution along the z-direction. Also, note that there are large deviations in chemical shift at the top and bottom corners of the sample with very high and very low frequency components, respectively, on the scale of ± 100 Hz.

A. *Line-Narrowing*

As Fig. 3 through Figs. 4a and 4b show, iZQCs significantly narrow linewidths in the indirectly detected dimension. In each figure, the conventional one-quantum signal overlays the indirectly detected dimension (F_2) spectrum. Figures 3a and 4a show a 50-Hz linear gradient along the z-axis, while Figs. 3b and 4b show the spectrum of a sample with a Gaussian distribution ($\sigma = 25$ Hz) along the z-axis. The proton resonance frequency in Fig. 3 is 165 MHz, which corresponds to a field strength of 3.9 T, while in Fig. 4 it is 600 MHz, or 14.7 T. The field strength only affects the signal amplitude, which is proportional to the magnetization for single-quantum (SQ) spectra, or the magnetization squared for iZQC spectra. The conventional signal of the linear offset has a distortion typical of the Fourier transformation of a function with sharp edges. The SQ signal in the two-component systems consists of only one resolvable peak (as the two components' peaks overlap significantly). The linear case has a FWHM linewidth of 75 Hz, while the Gaussian distribution gives a FWHM of 96 Hz.

In contrast to the broad unresolved lines of the SQC spectrum, the iZQC signal for Figs. 3a, 3b, 4a, and 4b show sharp lines. The FWHM for the axial peak in all three is approximately 6 Hz, very nearly the broadening due to the short total acquisition time imposed by computation time constraints. The cross peaks in Fig. 4, signal from the terms I^+S^- and I^-S^+, have FWHM linewidths of 6 Hz as well.

Figure 5 shows the iZQC signal for a solvent–solute sample. Figure 5a is from an iZQC CRAZED pulse sequence for the

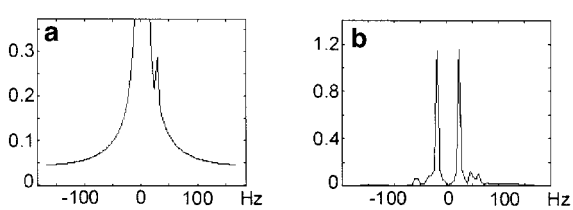

FIG. 5. (a) iZQC CRAZED spectrum for a solvent–solute system (111 M solvent/1 M solute) with no inhomogeneous broadening. (b) A 90–Gz–τ_{zq}–90 pulse sequence for 50-Hz line-broadened solvent–solute system efficiently suppresses the solvent peak at 0 Hz and allows clear resolution of the iZQC cross peaks at $\Delta\omega_{\text{solvent}} - \Delta\omega_{\text{solute}}$ (-25 Hz) and $\Delta\omega_{\text{solute}} - \Delta\omega_{\text{solvent}}$ (25 Hz).

sample under no inhomogeneous broadening. In the presence of a 50-Hz inhomogeneous broadening, the cross peak was no longer resolvable because of the overlap with the tail of the strong solvent peak. In order to compensate for this impediment, a 90_x pulse replaced the usual 45_x pulse in the iZQC CRAZED pulse sequence. Under the action of this 90_x pulse, the zero-quantum operators that create the axial peak are turned into unobservable terms,

$$I_{y1}I_{y2} + I_{x1}I_{x2} \xrightarrow{90_x} I_{z1}I_{z2} + I_{x1}I_{x2} \xrightarrow{H_{dij}} 0. \quad [28]$$

$I_{z1}I_{z2}$ represents longitudinal two-spin order, and $I_{x1}I_{x2}$ commutes with the dipolar Hamiltonian. The only terms that survive are from chemically inequivalent spins,

$$I_yS_x - I_xS_y \xrightarrow{90_x} I_zS_x - I_xS_z \xrightarrow{H_{dij}} I_y - S_y. \quad [29]$$

As noted above for the iZQC CRAZED, this imaginary component would be destroyed by phase cycling the second RF pulse, so only the first pulse was phase cycled, leaving this type of spectrum vulnerable to T_1 artifacts. Nevertheless, Fig. 5b shows very efficient suppression of the homonuclear same-spin signal and clearly resolved solvent–solute cross peaks in a strongly inhomogeneous field.

B. Sensitivity to Structure of the Inhomogeneous Broadening

There is no qualitative difference observed between the iZQC response to Gaussian or linear field variation, although the differences may become more apparent as the inhomogeneity is significant enough to be seen through the signal truncation broadening.

One difference to which the iZQC was quite sensitive was the direction of the inhomogeneous line broadening relative to the correlation gradient. When the correlation gradient and the inhomogeneous line broadening both are linear gradients, aligned on the *z*-axis, and operating in opposite senses, there is a significant artifact in the FID. When the area under the correlation gradient is matched by the integral of the chemical shift offset, the inhomogeneous broadening unwraps the magnetization helix established by the correlation gradient, destroys the possibility of observing MQCs, and removes the single-quantum filter.

When the offset is perpendicular to the correlation gradient, the direction of the magnetization helix (hence the DDF strength) becomes time dependent. The iZQC linewidths for samples under *x*-axis inhomogeneous broadening are much broader (~20 Hz, no cross peak resolved) because while the correlation gradient modulates the magnetization in *z*-direction (i.e., $k_z \neq 0$), the inhomogeneous broadening gives a modulation along the *x*-axis (and hence a nonzero k_x component). Because the offset continually effects the spins, the k_x component steadily increases in value throughout the experiment. When $k_x = 1.4\ k_z$, then the effective axis for the modulation is the magic angle and the first term in the dipolar field, Eq. [13], equals zero, destroying the iZQC signal.

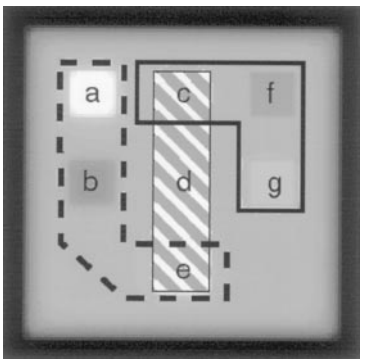

FIG. 6. The phantom used in the iZQC imaging simulations (magnetization summed along the *z*-axis). The sample is 64 by 64 by 32 grid points in the *x*, *y*, and *z* directions. Each block (a–g) is an 8 by 8 by 8 cube inside the background material. Areas inside the dashed line have spin density variations (M_0), areas inside the solid line have T_2 variations, and the blocks under the striped box have a 25-Hz chemical shift variation. The background has a relative density of 0.5, a chemical shift of 0 Hz, and a T_2 of 100 ms. Area (a) relative density 1, (b) relative density 0.25, (c) offset 25 Hz and T_2 50 ms, (d) offset 25 Hz, (e) offset 25 Hz and density 1, (f) T_2 50 ms, and (g) T_2 200 ms.

V. CRAZED IMAGING

A. Intermolecular Zero-Quantum Sequences

Contrast in conventional images is dominated by spin density and relaxation times. The CRAZED sequence provides several unique contrast features, as recently reported (*14*). For example, as noted in Ref. (*14*), iZQC signal is expected to come from pairs of spins separated by approximately the correlation distance $d_c = \pi/(\gamma GT)$, where GT is the area of the correlation gradient pulse. Thus localized resonance frequency variations on this distance scale contribute contrast. This is particularly important *in vivo*, because tissue oxygenation levels determine the resonance frequency. In addition, in typical applications this correlation distance is 50–500 μm, far smaller than typical voxel dimensions.

This set of calculations compares the relative effects of these three parameters (spin density, T_2, and resonance frequency variation) in a simulated phantom. The bulk of the sample (64 by 64 by 32 grid) has the following default values: relative spin density of 0.5, a chemical shift of 0 Hz, and a T_2 of 100 ms. The phantom, however, is divided into nine different areas, seven of which contain a subvolume (8 by 8 by 8) with parameters differing from the bulk. Figure 6 describes each of these inhomogeneities. The three regions under the dashed line contain a spin density variation, the three regions under the

solid line have a T_2 variation, and the three under the striped box have a 25-Hz chemical shift offset. The correlation gradient establishes three helices across the z-axis of the sample (eight points per helix, $d_c \sim 150$ μm). Note that the edge of each cube is one helix apart from its neighbors to prevent cube to cube interactions.

i. iZQC CRAZED images. The iZQC signal depends on the square of the magnetization ($\propto M_0^2$) and therefore emphasizes features with high spin density more than does a conventional image. Each block in Fig. 6 is $\frac{1}{3}$ of the total slice thickness. In a conventional image, such a block with double the spin density and would provide a signal $1\frac{1}{3}$ times the background. In the CRAZED experiment, the areas with additional spin density are more than twice as bright as the background. In addition, because the signal comes from two-spin terms, the signal from areas with a variation in spin density shows a rounded profile. This profile extends approximately one half-helix pitch (i.e., four points) beyond the edge of each cube, verifying that each cube should be nearly independent of its neighbors and will only interact strongly with the nearby background.

Because the signal derives from two-spin operators, the iZQC signal decays at $T_2/2$, twice as fast as conventional magnetization. Areas with shorter T_2 show less signal at long τ_{zq}, while longer T_2 areas keep more of their signal. Again, there is some small transfer of this signal intensity to the surrounding grid points.

The most interesting source of contrast observed in the CRAZED images is resonance frequency variation. As Fig. 7 shows, areas c, d, and e each have a ring around them whose intensity varies with τ_{zq}. This ring is at its most negative when the difference between spins' precession, $t_1(\Delta\omega_I - \Delta\omega_S)$, is π rad (i.e., $\tau_{zq} = 20$ ms). In order to see this evolution more clearly, a simpler sample was run (Fig. 8) with only a chemical shift difference in a central cube. At $\tau_{zq} = 0$ the ring around the inhomogeneity shows nearly no change. By $\tau_{zq} = 20$ ms the signal from this ring has fallen to two-thirds the level of the rest of the sample, leaving a "moat" of sorts around the center of the block. The width of this moat is approximately four grid points, again one half-helix pitch, emphasizing that the evolution is due to the chemical shift difference of two distant spins.

ii. The iZQC modCRAZED image. The modCRAZED image gives results which are very similar to those of the iZQC CRAZED images, with the exception of the chemical shift information. Where the iZQC CRAZED images show pronounced signal loss near the borders of areas with different chemical shifts, the simulations show that the π pulse in τ_{zq} refocuses most of the signal, in agreement with the one-dimensional calculation in Eq. [8]. There are, however, small dips around areas c, d, and e (Fig. 7) where the magnetization is not completely refocused. This imperfect refocusing is most likely due to the limited number of grid points near the borders between the cubes and the background, creating small differences in evolution before and after the π pulse. Other than this consideration, the modCRAZED experiment gives contrast based entirely on magnetization (again $\propto M_0^2$) and T_2.

iii. Subtraction images. Subtracting the CRAZED and the modCRAZED substantiates the qualitative prediction made by Eq. [9]. The only signal remaining in the images comes from chemically inequivalent spins separated one half pitch of the magnetization helix. Figure 9 shows the subtraction at three times the intensity scale of the CRAZED and modCRAZED images. The subtraction image is almost completely specific to areas that contain spins with different offset frequencies. The total width of the excited areas in the subtraction is four points, and the signal in these areas is positive and real at all points in the sample.

The observed maximum in the subtraction signal is at $\tau_{zq} = 20$ ms, in agreement with the prediction that the real part of the signal would have a $1 - \cos(t_1(\Delta\omega_I - \Delta\omega_S))$ dependence, and reaches a peak value of one-third the CRAZED signal. Experimentally observed iZQC CRAZED signals have a signal strength of several percent of a conventional image and a signal-to-noise ratio (SNR) of about 30 to 1 in human brain images at 4 T (*15*). This set of calculations predicts an observable (although small) signal from this subtraction, with a SNR of about 14 to 1. The SNR is reduced by a factor of 3 because of the smaller signal, but improved by $\sqrt{2}$ from the additional signal averaging.

B. Intermolecular Double-Quantum Imaging

The first demonstration that dipolar field effects could reveal sample structure was published in Ref. (*16*), which showed that iDQCs could be created between molecules in separated tubes, as long as the correlation distance was greater than the separation between the tubes. Reference (*17*) used Fourier decomposition of the magnetization to explore multiple echo effects in arbitrarily shaped samples. The first *in vivo* iDQC images, published in Ref. (*18*), give much lower quality images than our iZQC work and had little contrast. This result would have been anticipated from a simplistic treatment, because iDQCs evolve at the sum of the resonance frequencies, hence they would be expected to have much larger inhomogeneous broadening than conventional resonances and would not reveal spatial structure. In contrast, our iZQC images (*12, 15*) gave good signal-to-noise ratios and contrast which was demonstrably different from T_2 or T_2^*.

In reality, the reason for the failure of the experiments in Ref. (*18*) was more complex. That paper noted the existence of a sharp echo when the delay after the second pulse was twice the delay between the first two pulses. This unintuitive feature can be readily understood. After the first RF pulse a double-quantum coherence between spins 1 and 2 ($I_{x1}I_{x2} -$

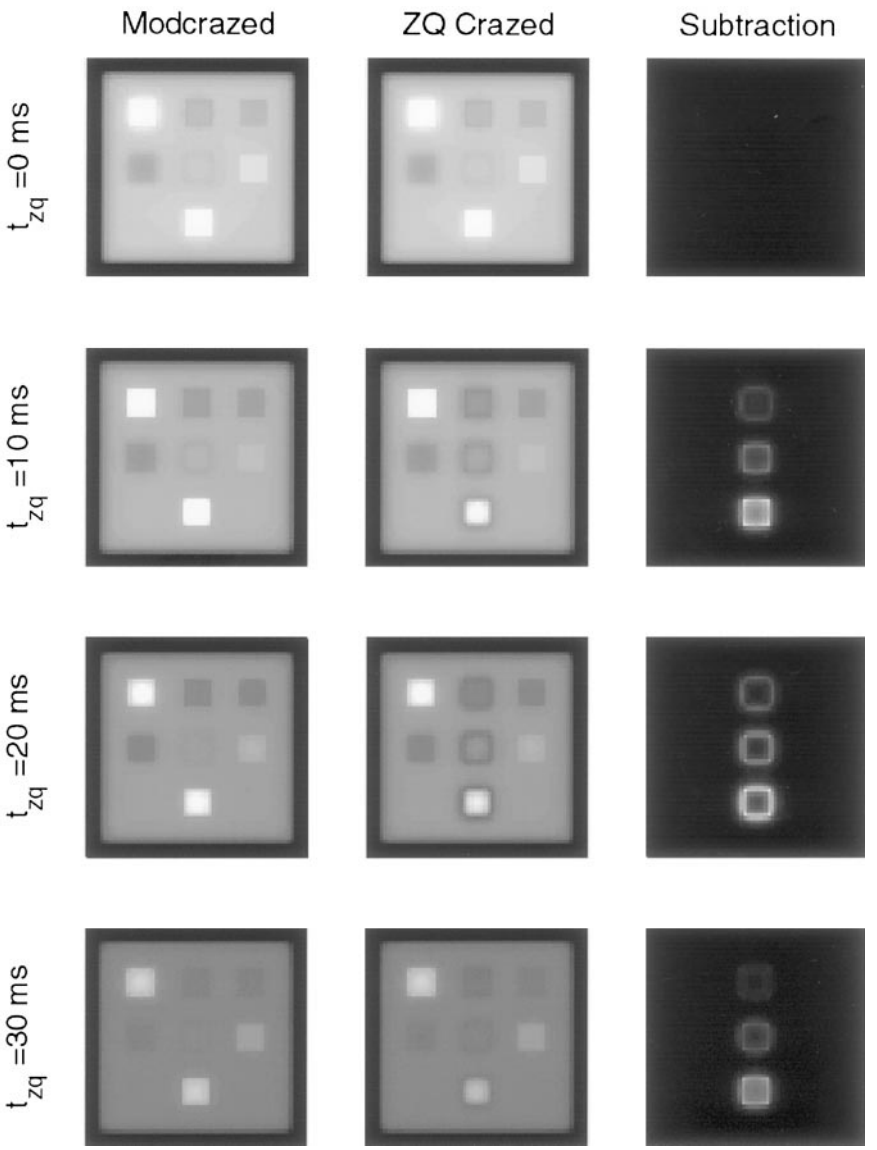

FIG. 7. Each image is M_x summed along the z-axis. The modCRAZED images show primarily contrast due to spin density ($\propto M_0^2$) and T_2. The iZQC CRAZED images show these as well as contrast from a difference in chemical shift between spins one half-helix pitch apart. This takes the form of dark rings around blocks (c–e). The subtraction (three times magnified scale) isolates signal from chemically inequivalent spins. This signal is at a maximum at $\tau_{zq} = 20$ ms, consistent with the $[1 - \cos(t_1(\Delta\omega_I - \Delta\omega_S))]$ prediction.

$I_{y1}I_{y2}$) evolves at the sum of the individual resonance frequencies ($\Delta\omega_1 + \Delta\omega_2$), for a duration of τ_{dq}. The second RF pulse transforms this into two-spin, single-quantum coherences, such as ($I_{x1}I_{z2} + I_{x2}I_{z1}$); those coherences evolve at the single-quantum frequencies $\pm\Delta\omega_1$ and $\pm\Delta\omega_2$, respectively. After a time interval of $2*\tau_{dq}$, the total phase evolution is $\pm\tau_{dq}*(\Delta\omega_1 - \Delta\omega_2)$, which depends only on the resonance frequency *difference* as in the iZQC case (even though the iDQC coherence itself evolves at the sum of the resonance frequencies). Reference (*12*) proposed a modified iDQC sequence (Fig. 1b), which has now been demonstrated to give iDQC functional images (*19*). The sequence at the lower right is the direct analog of the modCRAZED iZQC sequence, with added π pulses to prevent resonance frequency evolution; it has been used for human imaging as well (*20*).

Figure 10 compares iDQC and iZQC CRAZED images and modCRAZED images for the case $\tau = 10$ ms. Systematic exploration of the differences between iDQC and iZQC imaging will be presented elsewhere. Here we note that, in both cases, the modCRAZED images lose almost all contrast from resonance frequency variations. For example, the center square differs from its surroundings only in its resonance frequency and gives no contrast in the modCRAZED images; the edge contrast is retained in the two CRAZED images.

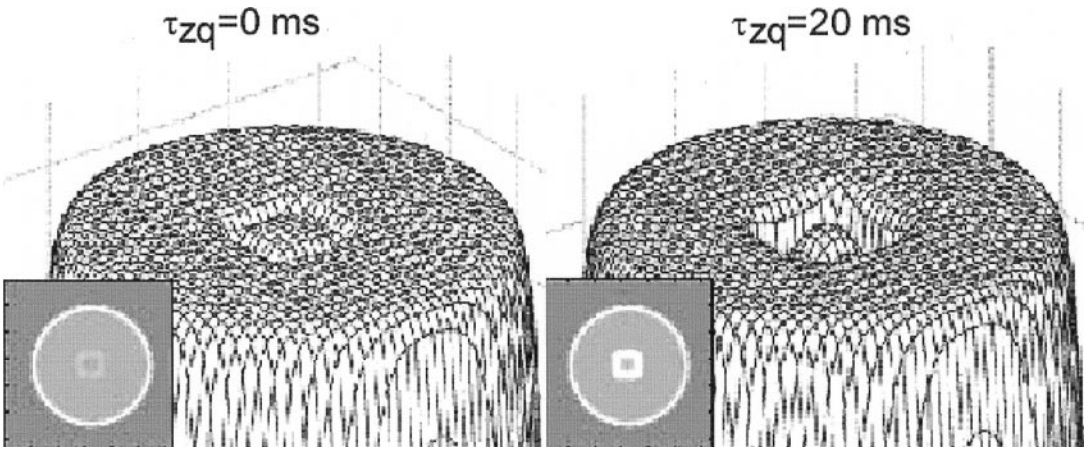

FIG. 8. Illustration of the contrast from chemically inequivalent spins. As chemical shift transfers signal from terms like I_yS_y to I_xS_x the observed amplitude decreases. This signal is only significant when spins with different chemical shifts are one half-helix apart (i.e., the four points at the edge of the inhomogeneity).

VI. DISCUSSION

A. Inhomogeneous Field High-Resolution NMR

This technique for improving the apparent homogeneity of the magnetic field is an exciting development. Table 1 gives predictions of the performance of iZQC CRAZED performance first scaled up to a 1-cm^3 sample, then to an inhomogeneous high field application. The samples simulated are 0.1 cm^3. Scaling their linear inhomogeneous broadening to a 1-cm^3 active area gives a total linewidth of 500 Hz. Unlike the conventional spectrum, which relies on the absolute homogeneity of magnetic field across the sample, the iZQC CRAZED spectrum depends only on the *relative inhomogeneity* of the sample over the 150-μm correlation distance, so its linewidth will not change with sample size. The iZQC spectrum has a line broadening of only 6 Hz when the inhomogeneity is along the *z*-axis and 20 Hz when it is along the *x*-axis.

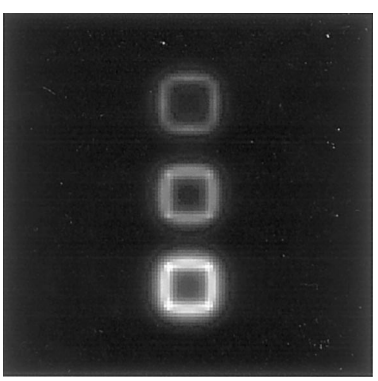

FIG. 9. Detail of the subtraction of the iZQC CRAZED from the modCRAZED experiment. Note that signal comes from the region at the edge of the inhomogeneity (one half-helix pitch). The signal intensity is one-third the iZQC CRAZED signal and scales with the number of chemically inequivalent spins.

This already significant gain should be even more pronounced in the high field application. Realistic numbers for one application (the 25-T Keck magnet at NHFML) are presented below. In predicting these values, note that the correlation distance was reduced to 50 μm (one-third the value in the simulation, but still significantly above the 10-μm diffusion barrier). Scaling the results from the simulation, in the presence of a 2 kHz/cm linewidth, the iZQC CRAZED sequence should provide a linewidth of 10 Hz for *z*-axis inhomogeneity and 30 Hz for *x*-axis inhomogeneity. This number nearly agrees with simple calculation based on the relative chemical shift difference between two spins 50 μm apart in this highly inhomogeneous field. In addition, the indirect dimension of the iZQC spectrum should be completely unaffected by drift in the magnetic field. Drift will affect detection of the iZQC signal, since it must eventually be converted into observable magnetization; fortunately, since the dipolar interaction is unaffected by echo pulse trains, it can be removed by a multiple-echo sequence.

B. iZQC/iDQC CRAZED Imaging and modCRAZED Subtraction

In general, iZQC or iDQC CRAZED imaging trades signal intensity for improved contrast. The most interesting additional source of contrast comes from localized resonance frequency variations; in addition, variations in magnetization density and relaxation times give stronger contrast here than in conventional images. The modCRAZED experiment is a variant of iZQC or iDQC imaging that removes contrast from resonance frequency variation and thus is probably most interesting only for producing reference images. The subtraction in Fig. 7 (to first order, at least) eliminates contrast from spin density and relaxation parameters, leaving only contrast from chemical shift differences on the distance selected by the correlation gradient.

In addition to a fundamentally new source of contrast, the

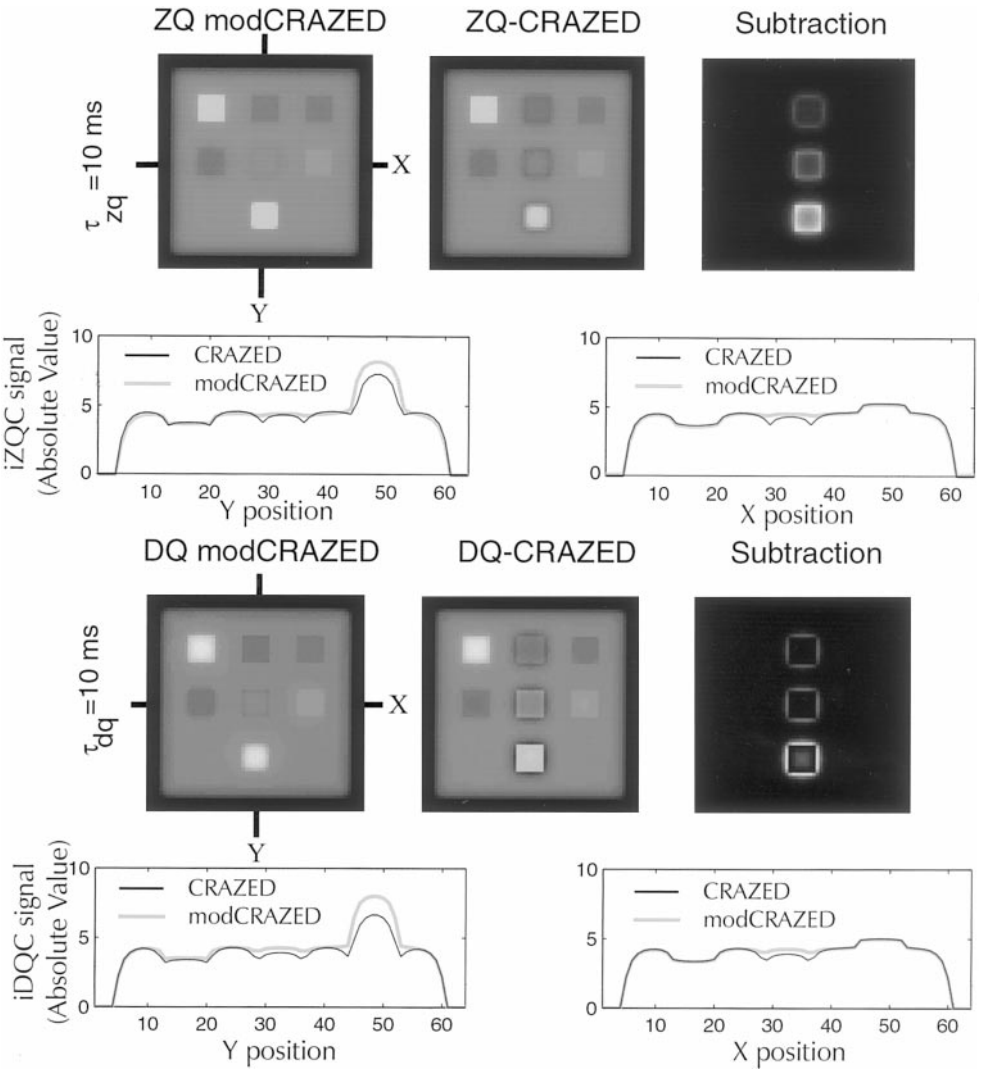

FIG. 10. Comparison of iDQC and iZQC CRAZED imaging experiments, and slices through three blocks in the structure. The "Y" slices are through the blocks with different resonance frequency (see Fig. 6); the "X" slices sample variations in T_2, density, and resonance frequency. Images have been adjusted to maximize contrast for feature comparison. Note that the modCRAZED images in either case remove the CRAZED edge contrast from local resonance frequency variations.

CRAZED image offers a new scale of "resolution." Although the actual resolution of the image is limited by sensitivity, the iZQC-CRAZED experiments can specify the distance between correlated spins. This specificity can be resolved one or two orders of magnitude more finely than conventional images.

The modCRAZED subtraction experiment has the same source of contrast as an iZQC CRAZED experiment but presents this contrast in what may be a more practical way. The imaginary component from the iZQC CRAZED pulse sequence also only comes from chemically inequivalent spins, but it can be difficult to realize the information it carries due to the symmetry of the imaginary component. The second RF pulse and the dipolar field create observable magnetization of the form (including evolution in t_1),

$$\sum_{ij} [I_{yi}\sin(t_1(\Delta\omega_I - \Delta\omega_S)) + S_{yj}\sin(t_1(\Delta\omega_S - \Delta\omega_I))]. \quad [30]$$

In the case of a full two-dimensional experiment, these terms would also be modulated by each spin's frequency in t_2, but this t_2 evolution is refocused in imaging. Because sine is an odd function, the total imaginary component of the observed signal cancels when the number of spins i is equal to j. There is one possible way around this—to separate the I and S spins, giving a signal profile with a dispersive peak shape. If, however, the spatial resolution (voxel size) in the image is too coarse to separate the I and S spins, then the positive and negative lobes of this peak will destructively interfere.

TABLE 1

		SQC spectrum (1 cm^3)	iZQC spectrum (1 cm^3)
Simulation (d_c[a] = 150 μm, 600 MHz)	Linewidth		
	(z)	500 Hz	6 Hz
	(x)	500 Hz	20 Hz
	Drift/h	0 Hz	0 Hz
Prediction (d_c = 50 μm, 1.07 GHz)	Linewidth		
	(z)	2,000 Hz	10 Hz
	(x)	2,000 Hz	30 Hz
	Drift/h	1,000 Hz	0 Hz

[a] d_c is the correlation distance.

The signal from the subtraction experiment, however, has even symmetry and so does not cancel. Even if spatial resolution is insufficient to resolve all the fine features of a sample (details on the scale of a grid point in these simulations), there should be a differential signal increase in the voxels that contain chemically inequivalent spins separated by the correlation distance. This phenomenon could possibly be treated in a manner similar to fMRI images, using the small increases in signal to make activation maps.

VII. CONCLUSIONS

These simulations have shown that iZQCs provide a potentially very powerful method for removing residual inhomogeneous broadening in electromagnets, using parameters that approximate the expected distributions from real magnets. They also show that iZQC imaging really does produce fundamentally different contrast than does conventional imaging. They suggest useful extensions of existing sequences as well.

ACKNOWLEDGMENTS

This work was supported by the NIH under Contract GM35253 and by the National Science Foundation through the NHFML Visitors program.

REFERENCES

1. Q. He, W. Richter, S. Vathyam, and W. S. Warren, *J. Chem. Phys.* **98,** 6779 (1993).
2. W. S. Warren, W. Richter, A. H. Andreotti, and S. Farmer, *Science* **262,** 2005 (1993).
3. S. Ahn, W. S. Warren, and S. Lee, *J. Magn. Reson.* **128,** 114 (1997); S. Ahn, S. Lee, and W. S. Warren, *Mol. Phys.* **95,** 769 (1998).
4. G. Deville, M. Bernier, and J. M. Delrieux, *Phys. Rev. B* **19,** 5666 (1979).
5. S. Ahn, S. Lee, and W. S. Warren, *Mol. Phys.* **95,** 769 (1998).
6. S. Lee, W. Richter, S. Vathyam, and W. S. Warren, *J. Chem. Phys.* **105,** 874 (1996).
7. See, for example, P. Robyr and R. Bowtell, *J. Chem. Phys.* **106,** 467 (1997); P. C. M. van Zijl, M. O. Johnson, S. Mori, and R. E. J. Hurd, *J. Magn. Reson. A* **113,** 265 (1995); I. Ardelian, R. Kimmich, S. Stapf, and D. E. Demco, *J. Magn. Reson.* **127,** 217 (1997); G. J. Bowden, T. Heseltine, and M. J. Prandolini, *Chem. Phys. Lett.* **233,** 639 (1995); M. Augustine and K. Zilm, *J. Magn. Reson. A* **123,** 145 (1996).
8. W. Richter, S. Lee, W. S. Warren, and Q. He, *Science* **267,** 654 (1995).
9. J. Jeener, A. Vlassenbroek, and P. Broekaert, *J. Chem. Phys.* **103,** 1309 (1995).
10. W. S. Warren and S. Ahn, *J. Chem. Phys.* **108,** 1313–1325 (1998).
11. S. Vathyam, S. Lee, and W. S. Warren, *Science* **272,** 92–96 (1996).
12. W. S. Warren, S. Ahn, M. Mescher, M. Garwood, K. Ugurbil, W. Richter, R. Rizi, J. Hopkins, and J. Leigh, *Science* **281,** 247 (1998).
13. T. Enss, S. Ahn, and W. S. Warren, *Chem. Phys. Lett.* **305,** 101 (1999).
14. S. Ahn, T. Enss, S. Garrett-Roe, Y. Lin, and W. S. Warren, ENC 1999 poster session.
15. R. R. Rizi, S. Ahn, D. C. Alsop, S. Garrett-Roe, M. D. Schnall, J. S. Leigh, and W. S. Warren, *Mag. Reson. Med.* **43,** 627 (2000).
16. W. Richter, Q. He, S. Lee, and W. S. Warren, *Science* **267,** 654 (1995).
17. R. Bowtell and P. Robyr, *Phys. Rev. Lett.* **76,** 4971 (1996).
18. S. Mori, R. E. Hurd, and C. M. van Zijl, *Magn. Reson. Med.* **37,** 336–340 (1997).
19. W. Richter, M. Richter, W. S. Warren, H. Merkle, P. Andersen, G. Adriany, and K. Ugurbil, *Magn. Reson. Imaging* **18,** 489 (2000).
20. J. Zhong, Z. Chen, and E. Kwok, *Magn. Reson. Med.* **43,** 335 (2000).